



저작자표시-비영리-변경금지 2.0 대한민국

이용자는 아래의 조건을 따르는 경우에 한하여 자유롭게

- 이 저작물을 복제, 배포, 전송, 전시, 공연 및 방송할 수 있습니다.

다음과 같은 조건을 따라야 합니다:



저작자표시. 귀하는 원저작자를 표시하여야 합니다.



비영리. 귀하는 이 저작물을 영리 목적으로 이용할 수 없습니다.



변경금지. 귀하는 이 저작물을 개작, 변형 또는 가공할 수 없습니다.

- 귀하는, 이 저작물의 재이용이나 배포의 경우, 이 저작물에 적용된 이용허락조건을 명확하게 나타내어야 합니다.
- 저작권자로부터 별도의 허가를 받으면 이러한 조건들은 적용되지 않습니다.

저작권법에 따른 이용자의 권리는 위의 내용에 의하여 영향을 받지 않습니다.

이것은 [이용허락규약\(Legal Code\)](#)을 이해하기 쉽게 요약한 것입니다.

[Disclaimer](#)

Master's Thesis of Science Education

Source parameters estimation of the 2020 Monte Cristo Range earthquake using InSAR

InSAR를 이용한 2020 Monte Cristo Range
지진의 진원 파라미터 추정

August 2023

Graduate School of Science education
Seoul National University
Earth Science Major

Sinae Kim

Source parameters estimation of the 2020 Monte Cristo Range earthquake using InSAR

지도 교수 서 기 원

이 논문을 교육학석사 학위논문으로 제출함
2023년 7월

서울대학교 대학원
과학교육과 지구과학전공
김 신 애

김신애의 교육학석사 학위논문을 인준함
2023년 8월

위 원 장	김 덕 진	(인)
부위원장	서 기 원	(인)
위 원	전 태 환	(인)

Abstract

In mitigating damages associated with earthquakes, it is necessary to understand the mechanism of earthquakes. Studying earthquake source parameters such as epicenter locations, focal depths, and magnitudes is crucial in understanding the mechanism of earthquakes. Since recent advances in InSAR allow us to construct high-resolution maps of coseismic surface displacement fields, InSAR has been efficiently utilized in earthquake studies. In this study, InSAR data is used to estimate the coseismic displacement field and the source parameters of the 2020 Monte Cristo Range earthquake and then the epicenter location, strike, dip, length, width, and focal depth of the fault by the Monte Carlo method. The slip vector is estimated by inversion using the fault model. The estimation presented oblique-slip, including dominant east-northeast (ENE) trending left-lateral strike-slip faulting with minor normal dip-slip faulting. The estimated earthquake location coincided with the observation better than that of other moment tensors. The estimated optimal focal depth and moment were quite shallower and smaller than those of other moment tensors, but a similar agreement can be obtained from the deeper focal depths and the longer fault width. In this study, the utility of InSAR for inferring Source parameters is verified. It is expected to obtain more accurate source parameters if Source parameter studies are conducted using both InSAR and seismic waveform data for various earthquakes.

Keyword: Earthquake, InSAR, Source parameter, Inversion
Student Number: 2019-22192

Contents

Chapter 1. Introduction	1
Chapter 2. Background.....	4
2.1 Earthquake source parameters	4
2.2 Principle of InSAR	7
2.3 Geological banckground of the study area	9
Chapter 3. Data and Methods	11
Chapter 4. Results.....	14
Chapter 5. Discussion and Conclusions.....	22
Reference	24
Abstract in Korean	27

List of Figures

Figure 1. Fault geometry used in earthquake studies	4
Figure 2. Coseismic displacement fields of a left-lateral strike-slip fault ...	5
Figure 3. SAR geometry for 3-D displacement estimation	8
Figure 4. Simple tectonic map of western US	9
Figure 5. Proposed models describing fault slip across the Mina deflection	10
Figure 6. Interferograms of images taken before and after the earthquake and images taken atfer the arthquake	14
Figure 7. LOS and 3-D displacement fields of the earthquake	15
Figure 8. The epicenter locations estimated from InSAR and moment tensors.	16
Figure 9. RMS in the variation of the fault length, width, and focal depth variation.	17
Figure 10. The observed and estimated displacement fields and residuals.	18
Figure 11. The horizontal, vertical displacement fields, and fault dimension in cross section of inferred from Moment tensors.	21

List of Tables

Table 1. The interferometric pairs used in this study.....	11
Table 2. The estimated focal depth, and fault geometry inferred from InSAR and moment tensors	19
Table 3. . The estimated fault dimension, slip, moment, magnitude, and RMS inferred from InSAR and moment tensors.	20

Chapter 1. Introduction

Earthquakes are one of the most hazardous natural phenomena on Earth. From 1980 to July 2022, six out of the ten deadliest natural disasters were due to earthquakes, and the most significant natural disaster caused 220,000 dead by the tsunami was generated by the 2004 Indian Ocean earthquake (Statista Search Department, 2022). In mitigating damages associated with earthquakes, it is necessary to understand the mechanism of earthquakes. Studying earthquake source parameters such as epicenter locations, focal depths, and magnitudes is crucial in understanding the mechanism of earthquakes.

Since the 20th century, seismic waveforms have been commonly used to estimate earthquake source parameters. However, the estimates include significant uncertainties. For example, global earthquake catalogs made by seismic data typically show about 10 km of uncertainty in the estimations of epicenter locations and about 25 km of uncertainty in the estimations of focal depths due to measurements errors of arrival times, modeling errors of seismic wave velocity, and nonlinearity of the earthquake location problem (Husen & Hardebeck, 2010). Further, they show moment magnitude variations derived from empirical correlations with conventional magnitudes because each catalog uses different types of seismic waves. For example, the Harvard Centroid Moment Tensor uses body waves with periods greater than 45 seconds and long-period mantle waves for events with larger magnitude; on the other hand, the US Geological Survey (USGS) Moment Tensor uses W-phase, long-period (~100-2000s) body-waves, and long-period (~20-200s) surface waves (Kagan 2022).

On the other hand, there are many studies using geodetic observations, including Global Positioning System (GPS) and Interferometric Synthetic Aperture Radar (InSAR), for earthquake source parameter estimations. In particular, recent advances in InSAR allow us to construct high-resolution maps of coseismic surface displacement field with a precision of ± 1 cm in low vegetation with a short temporal baseline (Dawson & Tregoning, 2007; Simons et al., 2002; Wright et al., 2003). Since Massonnet et al. (1993) successfully showed that the displacement of Landers earthquake mapped by InSAR agrees with the dislocation model, InSAR has been efficiently utilized in earthquake studies.

A surface displacement image inferred from InSAR is basically given as a projection onto the line of sight (LOS) vector of the satellite (i.e., one-dimensional displacements). The combination of ascending and descending orbits provided additional information to obtain three-dimensional displacements, and thus earthquake source parameters can be obtained from those displacement fields. These satellite geodetic observations have been used to understand earthquake source parameters, particularly around epicenters where GPS data is unavailable.

Here in this study, Source parameters are inferred by using InSAR techniques for the 2020 Monte Cristo range earthquake. On May 15, 2020, a magnitude 6.5 Monte Cristo range earthquake struck near the border of Nevada and California. The epicenter is within Walker Lane, which is believed to accommodate up to 25% of the relative motion between the North American and Pacific plates (Bennett et al., 2003). USGS reported The earthquake resulted from strike-slip faulting in the shallow crust of the North American plate, a depth of 2.7 km. As seismic waves have an ambiguity in distinguishing between the fault plane and the auxiliary plane, the moment tensor indicates the possibility of strike-slip faulting either on an east-west

trending fault (left-lateral) or on a north-south trending fault(right-lateral). The distribution of epicenters of aftershocks supports the former.

Since this area is dry and sparsely vegetated, it is expected to obtain suitable SAR images. Zheng et al. (2020) studied the source rupture process of the earthquake by applying joint inversion of InSAR and broadband seismic data and suggested a two-segment fault model. Chorsi et al. (2022) showed a series of slip models consistent with InSAR data. However, a detailed analysis of the earthquake source parameters of this event was rarely attempted.

In this study, InSAR data is used to estimate the coseismic displacement field and the source parameters of the 2020 Monte Cristo Range earthquake and then compared with the source parameters determined by seismological methods to evaluate InSAR data to determine earthquake source parameters. The earthquake source parameters estimated from InSAR observations are assumed to be more reliable than those from seismological data because InSAR provides *in situ* displacement fields. Global Centroid Moment Tensor (GCMT), USGS W-phase, USGS body-wave, and Nevada Seismic Network (NN) moment tensor are used for the seismological references.

Chapter 2. Background

2.1 Earthquake source parameters

Earthquakes usually occur on faults, breaks in the Earth's crust, where one side of the crust moves relative to the other. According to elastic rebound theory (Reid, 1910), friction on the fault prevents each side from slipping. It causes accumulation of strain in rocks until they fail to hold any more strain. The fault suddenly slips and releases accumulated energy in seismic waves, resulting in earthquakes.

For simplicity, a rectangular plane with a finite size is widely used to describe the fault segment. This model is useful for geometric understanding of fault parameters such as strike, dip, rake, and fault dimensions. Fault geometry is described with strike, dip, rake, and fault dimensions. Figure 1 shows the fault geometry of a finite fault plane model utilized in many earthquake studies. The strike of a fault is the direction of the line formed by the intersection of the fault plane with the surface. The dip of a fault is the inclined angle of the fault plane relative to the surface. The rake represents the direction of the fault slip vector motion of the hanging wall relative to the footwall. It is defined by the angle of the fault slip vector measured counterclockwise from the strike of the fault.

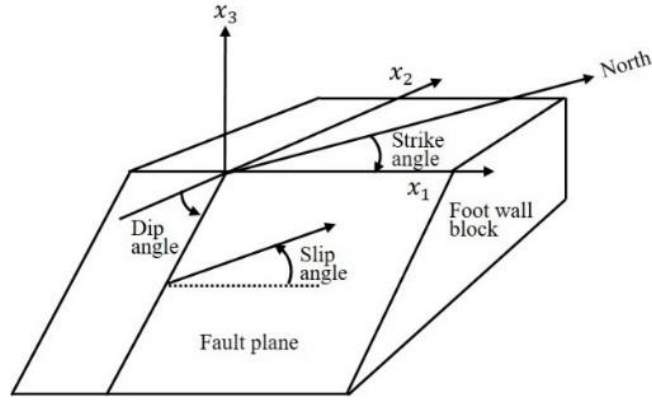


Figure 1. Fault geometry used in earthquake studies

(Modified from Stein and Wyssession, 2003).

The strike-slip and dip-slip faults represent purely horizontal and vertical motion of the fault along the fault plane, respectively. Thus, the combination of these two components can describe an arbitrary fault slip vector.

When a fault is treated as a rectangular fault plane with length and width, it is also convenient to evaluate the seismic moment. The seismic moment is determined by fault area (S), average slip (D), and shear modulus (μ) and used as a measure of released energy during an earthquake,

$$M_0 = \mu DS \quad (1)$$

The spatial pattern of coseismic surface displacements depends on the various fault parameters explained above. For example, Figure 2 shows coseismic displacement fields of a single left-lateral strike-slip fault segment.

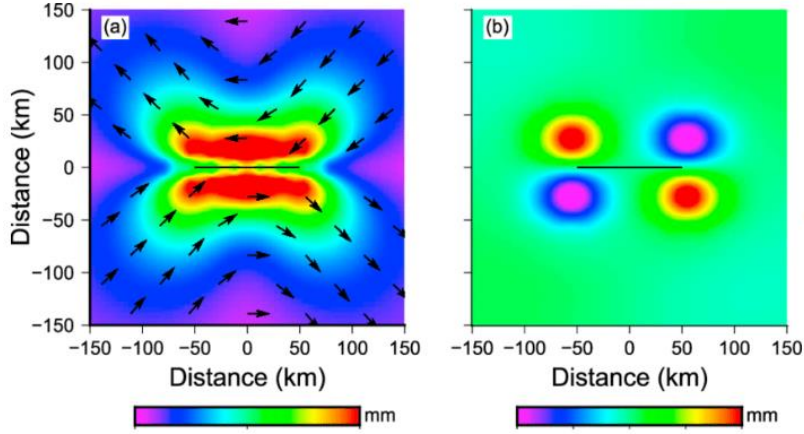


Figure 2. Coseismic displacement fields of a left-lateral strike-slip fault which is buried at a depth of 10~35km The seismic moment of fault is $6.6 \times 10^{21} N \cdot m$ (a) The horizontal component and (b) the vertical component (from Tang and sun, 2018).

Thus, from a fault model that provides similar responses at the surface, it is possible to estimate the fault parameters of the earthquake event. Besides, Total slip vectors can be estimated by linear inversion because those are the sum of strike-slip and dip-slip vectors, and slip vectors are linearly related to the surface deformation. This can be expressed as

$$d = Gm \quad (2)$$

where d , G , and m are surface displacements, unit slip vector displacements of strike-slip and dip-slip fault, and slip vector parameters, respectively. Surface displacements can be observed by geodetic systems such as SAR or GNSS, and unit slip vector responses can be obtained by fault model; therefore, slip vector parameters can be estimated by minimizing squared misfit (i.e., error).

$$m = (G'G)^{-1}G'd \quad (3)$$

when the other fault parameters associated with fault geometry are appropriately fixed.

2.2 Principle of InSAR

Earthquake geodesy is a technique of measuring ground deformation to obtain information about earthquakes. The basic geodesy technique is detecting objects' movement on the ground. Coseismic displacements can be obtained by geodetic data before and after earthquakes. There are various ways to collect geodetic data; Interferometric Synthetic Aperture Radar (InSAR) is one of them. SAR is a radar system that uses the synthetic aperture to map high-resolution ground images from aircraft or satellites. The transmitted radar pulse is scattered by the ground surface or object in the ground, and then parts of the pulse return to the receiver. Receiving radar pulse contains information about scatterers. Amplitude is related to backscattering intensity and phase to distance between radar and target. InSAR uses the phase difference of two SAR images, differential interferogram, for measuring displacements. The phase difference is proportional to range change and inversely proportional to wavelength.

$$\Delta\phi = \frac{4\pi}{\lambda} \Delta r \quad (4)$$

where λ is the wavelength and Δr is the range change between SAR and the target. If there is more phase change than 2π , repeated cycles of 2π are presented in interferogram showing a number of fringes. The interferogram, including phase fringes, is called wrapped phase difference map, and thus, phase unwrapping is necessary to obtain displacements (i.e., range change Δr) according to equation (2). These displacements are Line of Sight (LOS) displacements.

The LOS displacement (d_{LOS}) is the sum of projected horizontal and vertical displacements (d_E , d_N and d_Z) onto the LOS direction (Furhmann, 2019),

$$d_{LOS} = \begin{pmatrix} -\sin\theta\cos\alpha & \sin\theta\sin\alpha & \cos\theta \end{pmatrix} \begin{pmatrix} d_E \\ d_N \\ d_Z \end{pmatrix} \quad (5)$$

where θ is the incidence angle between the LOS direction and the normal to the surface, and α is satellite heading, also referred to as the azimuth of the satellite measured clockwise from North. Displacement vectors (d_E , d_N , and d_Z) can be estimated from multiple pairs of LOS displacements and equation (1). 3-D displacement vectors can be estimated via,

$$\begin{pmatrix} d_{LOS1} \\ d_{LOS2} \\ \vdots \\ d_{LOSn} \end{pmatrix} = \begin{pmatrix} -\sin\theta_1\cos\alpha_1 & \sin\theta_1\sin\alpha_1 & \cos\theta_1 \\ -\sin\theta_2\cos\alpha_2 & \sin\theta_2\sin\alpha_2 & \cos\theta_2 \\ \vdots & \vdots & \vdots \\ -\sin\theta_n\cos\alpha_n & -\sin\theta_n\cos\alpha_n & -\sin\theta_n\cos\alpha_n \end{pmatrix} \begin{pmatrix} d_E \\ d_N \\ d_Z \end{pmatrix} \quad (6)$$

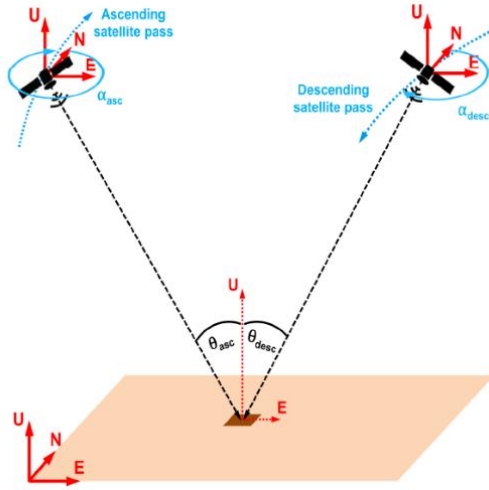


Figure 3. SAR geometry for 3-D displacement estimation (from Furhmann, 2019).

2.3 Geological background of the study area

The Eastern California Shear Zone (ECSZ)–Walker Lane Belt (WLB) is an NW dextral shear zone located near the border of California and Nevada, USA (DeLano et al., 2019). This shear zone includes many stepover zones, such as the Mina Deflection. Strike-slip faults commonly break into subparallel and non-coplanar segments. A stepover occurs between the end and the beginning of two strike-slip fault segments, where the strain of one fault transfer to the other. Due to this local deformation, short fault segments connecting adjacent two strike-slip fault segments are formed in a stepover zone. The Mina Deflection is a ~45km-wide and ~125km-long right-stepping zone that connects northern ECSZ to central WLB faults (Nagorsen-Rinke et al., 2013). Figure 4 shows the location of the Mina deflection and surrounding tectonic provinces.

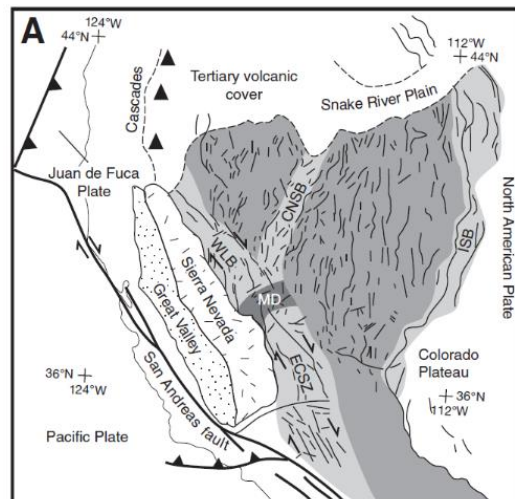


Figure 4. Simple tectonic map of western US showing the major faults, plates boundaries, and tectonic provinces; Walker Lane belt (WLB), Eastern California shear zone (ECSZ), and Central Nevada seismic belt is shaded in light gray; Mina deflection (MD) is shaded in dark grey; Basin and Range Province is shaded in medium grey (from Nagorsen-Rinke et al., 2005).

Faults within the Mina Deflection are north-northwest striking with right-oblique slip or east-west striking with left-oblique slip (Ferranti et al., 2009). Three models have been proposed demonstrating fault slip transfer across the Mina deflection (DeLano et al., 2019). (1) Oldow and Craig (1992) and Oldow et al. (1994) suggested a displacement-transfer model which explains that low-angle normal slip faults connect north-northwest striking transcurrent faults. (2) Oldow (2003) proposed another model explaining the connecting faults as both normal and sinistral slip faults, and (3) Nagorsen-Rinke et al. (2013) proposed a clockwise block rotation model with sinistral slip across the dextral slip faults.

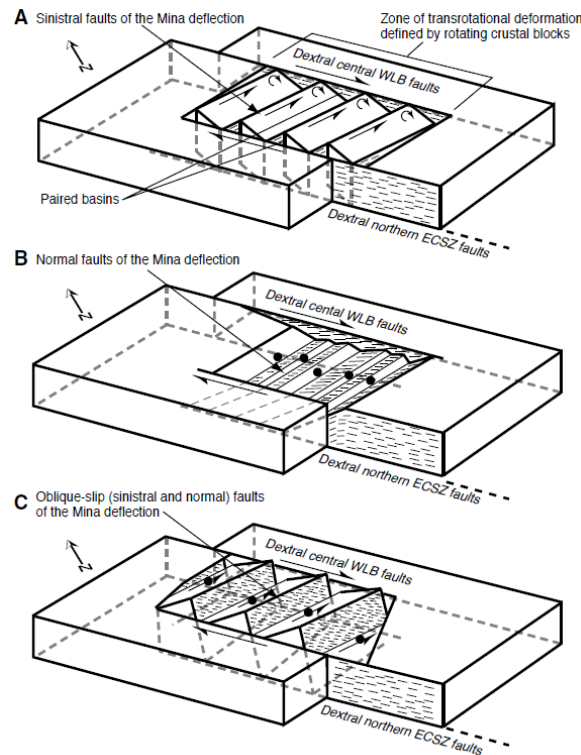


Figure 5. Proposed models describing fault slip across the Mina deflection. (A) The clockwise block rotation model. (B) The displacement-transfer model. (C) The normal and sinistral slip model (from DeLano, 2019).

Chapter 3. Data and Methods

Sentinel-1 Single Look Complex (SLC) images covering the study area are utilized, acquired from four ascending and four descending orbital tracks. The Sentinel-1, a constellation of two polar-orbiting satellites, performs C-band synthetic aperture radar imaging operated by European Space Agency (ESA). The default acquisition mode of Sentinel-1 over land is IW mode, which images three sub-swaths using Terrain Observation with Progressive Scans SAR (TOPSAR) covering a large swath width (250 km) with a geometric resolution of about 5 m by 20 m. Sentinel images can be freely downloaded from Alaska vertex (<https://vertex.daac.asf.alaska.edu>) or ESA Copernicus (<https://scihub.copernicus.eu>).

Table 1. The interferometric pairs used in this study.

Direction	Track	Frame	Acquisition date	Temporal baseline(d)	Perpendicular baseline(m)
Ascending	64	123 and 118	20200505-20200517	12	32
			20200511-20200523	12	-22
	64	119	20200429-20200523	24	60
			20200511-20200604	24	86
Descending	144	462	20200510-20200522	12	8
	144	466	20200504-20200516	12	-60
	71	463	20200505-20200517	12	-112
	71	465	20200511-20200523	12	92

Coseismic interferograms are constructed from four ascending and four descending orbit image pairs captured before and after the earthquake. The time interval between the two images used in the interferograms is 12 days, corresponding to the repeat period of the Sentinel-1. However, due to insufficient ascending orbit images

covering the study area, the interval is increased to 24 days in two ascending orbit image pairs. Table 1 presents the detailed properties of all data sets used in this study.

SNAP 7.0 software provided by ESA is utilized to produce the differential interferogram, which proceeds as follows:

- Coregistration: The first step is to apply the orbit file for fine co-registration. Next, Back-Geocoding is applied to modify slave images by DEM and interpolating complex values. BISINC_5_point_interpolation is applied, which is followed by enhanced spectral diversity (ESD) for more precise alignment.
- Interferogram formation: The interferograms are produced from the coregistered pairs before topographic phase removal and Goldstein phase filtering.
- Geocoding: Range Doppler Terrain correction is applied to geocode.

After producing the interferogram by SNAP software to obtain more clear fringes, Additionally, the low coherent phase is filtered using a threshold of 0.3 before applying the phase filtering that averages the phase over a 3×7 pixel window five times and then calculated LOS displacement from the unwrapped interferogram (Aebischer & Waldner, 1999; Ghiglia & Romero, 1994).

The least-square method is utilized to estimate robust horizontal and vertical displacements by minimizing observation error in LOS displacement. Horizontal and vertical displacements are solved for each pixel due to the change of incidence angle from the nearest to the farthest range, while the satellite heading is treated as a constant.

Based on the 3-D coseismic displacement fields, the epicenter location and the strike and dip of the fault are estimated by the Monte Carlo method. The fault is assumed as a single rectangular segment, and the tensile component is set to be zero. Here, the dislocation model of Okada (1985) is used, and the model provides the

surface displacements due to a finite rectangular seismic source placed in a homogeneous elastic half-space. Using the fact that coseismic displacements by a slip vector can be linearly decomposed into the effect due to strike-slip and dip-slip components, linear inversion is applicable to compute the slip vector. Here, this linear relationship is valid only when the other non-linear parameters such as position, size, focal depth, dip, and strike of the fault are fixed. Thus, numerous displacement fields of unit slip vectors (i.e., 1 m of strike-slip and dip slip vectors) were prepared considering the diverse non-linear fault parameters. Each case with various angle and size yields the fault slip vector by linear inversion, and the model prediction can be compared with the observed coseismic displacement fields. Based on the agreement between the observation determined by the RMS differences, the best fault parameters are found. Further, the result is compared with other surface displacement estimates from seismological model references.

Chapter 4. Results

The interferograms used in this study include displacements due to aftershocks. An interferogram of images taken the next day and after 24 days is made to identify the effect of aftershocks. Figure 6 shows the interferogram made by images taken before and after the earthquake and that made by both taken after the earthquake. The former has distinct fringes; however, the latter has one unclear fringe. Thus, phases of aftershocks in interferograms used in this study can be negligible.

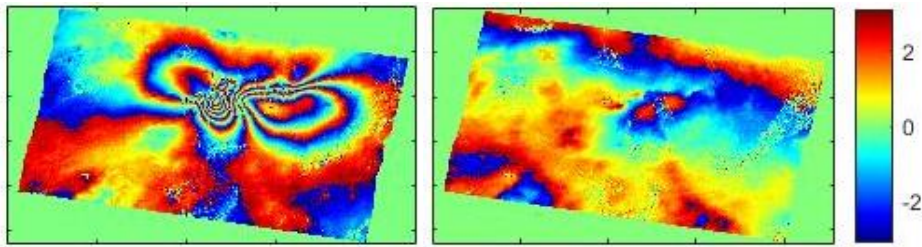


Figure 6. Interferograms of images taken before and after the earthquake (a) and images taken after the earthquake (b).

Figure 7 shows LOS displacement fields of ascending and descending orbit and three-dimensional displacement fields estimated from equation (4). The northing displacement field does not show apparent coseismic deformation due to noise contamination associated with the northing or southing satellite orbits, which results in the least sensitive northing measurements. Accordingly, only easting and vertical displacements are used for source parameter estimation. The easting displacement field shows a left-lateral strike slip on the fault, and the vertical displacement field shows that the slip also has a vertical component. The maximum displacement of horizontal and vertical components is 17 cm westward and 23 cm downward, respectively.

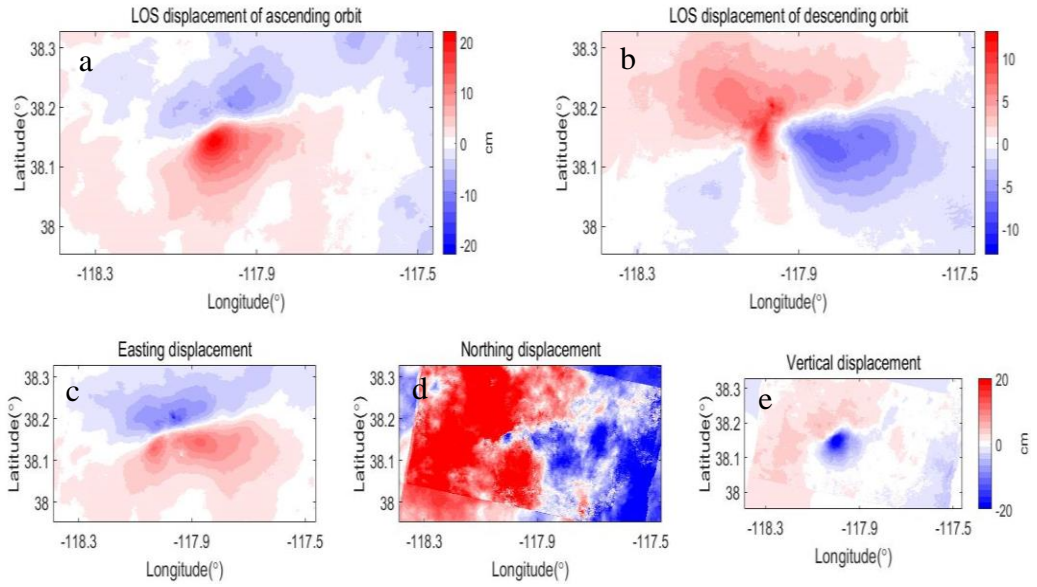


Figure 7. LOS D displacement fields from ascending (a) and descending orbit and 3- D displacement fields. (c–e)

Figure 8 shows the epicenter location of this study and moment tensors. The epicenters of seismological references are distant from each other. It is likely due to the uncertainty of the seismological method for determining the epicenter. The estimation of this study is closest to the epicenter of the W-phase moment tensor, and the distance is 1.4 km. The epicenters of the NN moment tensor and the Body-wave moment tensor are on the east side of the others. The epicenter of GCMT, the farthest one, is on the northeast side of our epicenter, and the distance is 7.6 km.

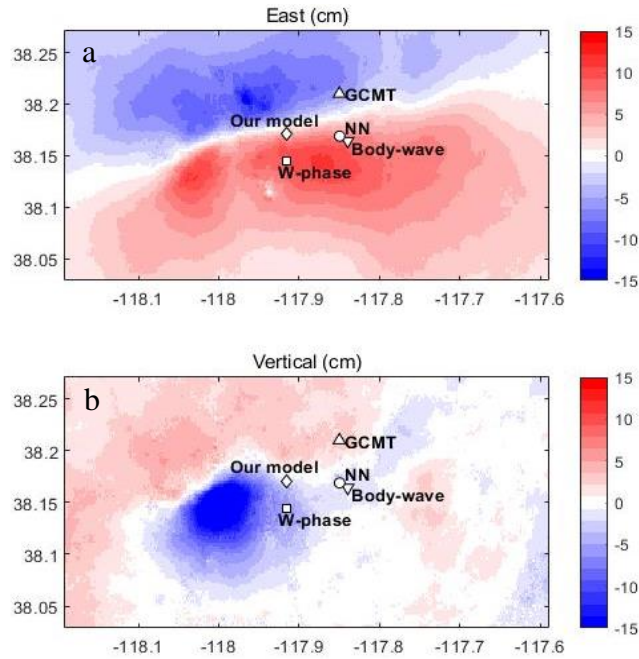


Figure 8. The epicenter locations estimated from InSAR and moment tensors in the easting (a) displacement field and the vertical (b) displacement field.

With the optimized epicenter location, the fault length, width, depth, dip, and strike are further examined by using the minimized the RMS difference (between model predictions and In-SAR observations). Here, the various model parameters were examined: strike from 60° to 90° , dip from 60° to 90° , fault length from 14 km to 24 km, the fault width from 6 km to 14 km, and the focal depth from 5 km to 13 km. These cases all provide the slip vectors and the corresponding model predictions. For example, Figure 9 shows RMS differences in the fault length, width, and focal depth variation when using the fixed strike and dip of 78° and 85° , respectively. The result shows that the lowest RMS differences are found in the several cases. It indicates a tendency that the fault width (along-dip length) and the focal depth are in a complementary relation. Among those similar relative minimum RMS, the minimum RMS is provided when the fault length, width, and focal depth are 20 km, 9 km, 7 km, respectively. Based on these experiment, the optimized fault parameters are provided when using the strike of 78° , the dip of 85° .

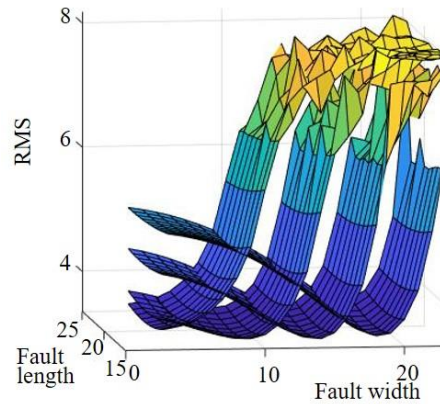


Figure 9. RMS in the variation of the fault length, width, and focal depth variation. Each plotted surface in the figure is for a focal depth of 5, 7, 9, and 11 km from the left.

Figure 10 shows the displacement fields from InSAR data, the model prediction, and the model misfits. They considerably coincide with the easting displacement field but is dissimilar in vertical displacement. It is due to significant subsidence in the epicenter's southwest area, but the model prediction does not include the signal.

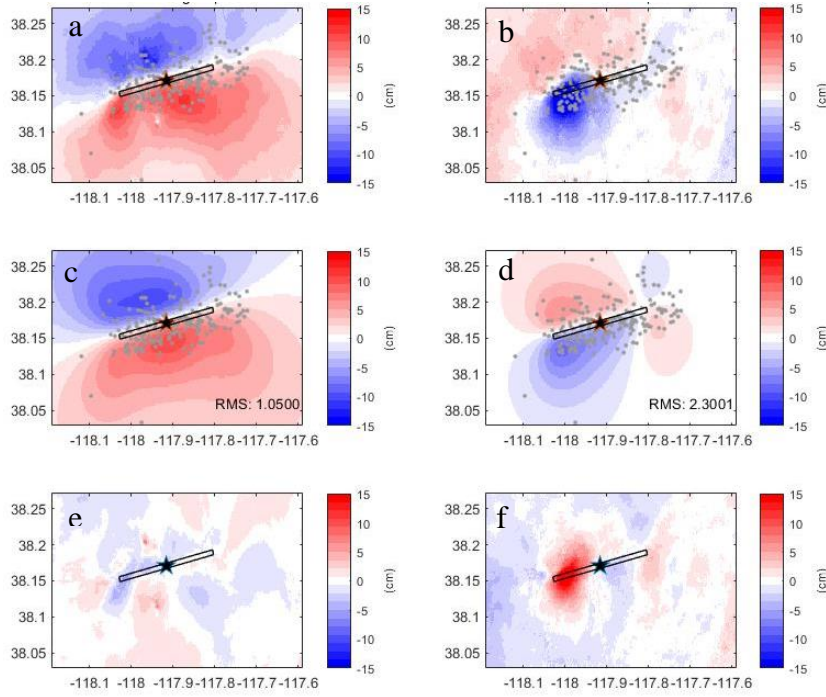


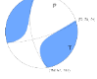
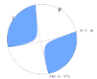



Figure 10. The observed(a–b) and estimated (c–d) easting and vertical displacement fields, and residuals(e–f). The black star represents the epicenter location, the gray dots are aftershock epicenters, and the black lined rectangle is the surface projection of the estimation.

Table 2 shows this study's moment, magnitude, depth, fault geometry estimation, and seismological references. The estimated depth is shallower than any other moment tensor. Moment tensors show similarity in depths, strikes, and dips. This estimation of this study and references all presented oblique-slip, including dominant east-northeast (ENE) trending left-lateral strike-slip faulting with minor normal dip-slip faulting except the NN moment tensor. NN moment sensor shows pure left-lateral strike-slip faulting. The estimated strike and dip correspond well with ones of the Body-wave moment tensor, whereas the estimated rake agrees most with the one of GCMT. Strikes and dips are generally similar, showing a variation of 5° and 7° each, but rakes show a variation of 24° .

Table 1. The estimated focal depth, and fault geometry inferred from InSAR and moment tensors. The beach balls are from each moment tensor web pages.

	Depth (km)	Strike ($^\circ$)	Dip ($^\circ$)	Rake ($^\circ$)	Beach ball
The estimation inferred from InSAR	7	78	85	-14	
GCMT	12	75	81	-16	
USGS (W-phase)	11.5	73	78	-24	
USGS (Body-wave)	11	78	85	-4	
NN	10	78	83	0	

Fault dimensions are missing from the reference moment tensors; thus, the fault dimensions of the reference moment tensors are constrained for comparison. Depth, strike, dip, and rake moment of each moment tensor are utilized to compute displacement fields resulting from unit slip vectors with variations in fault dimensions. Subsequently, the total slip vector is estimated through linear inversion, combining observed coseismic displacement fields. Table 3 shows fault dimensions, slip, and RMS.

Table 2. The estimated fault dimension, slip, moment, magnitude, and RMS inferred from InSAR and moment tensors. The RMS is the difference between the observation and the estimation of the easting and vertical displacement fields.

	Length (km)	Width (km)	Slip (m)	Moment ($10^{18}Nm$)	Magnitude (M_w)	RMS(E)	RMS(V)
The estimation inferred from InSAR	20	9	0.63	3.67	6.34	1.05	2.30
GCMT	31	10	0.69	6.34	6.50	3.31	2.72
USGS (W-phase)	28	19	0.39	6.77	6.52	2.07	3.28
USGS (Body-wave)	16	20	0.43	4.33	6.39	1.58	2.77
NN	23	18	0.43	3.28	6.28	2.42	3.09

Fault dimensions and moments vary considerably. Figure 11 shows displacement fields from source parameters in Table 2 and 3. The displacement fields of reference moment tensors considerably are deviated from the observation and produce large RMS. It is likely due to the poorly located epicenter because RMS of moment tensors decreased when using the estimated epicenter location inferred from InSAR.

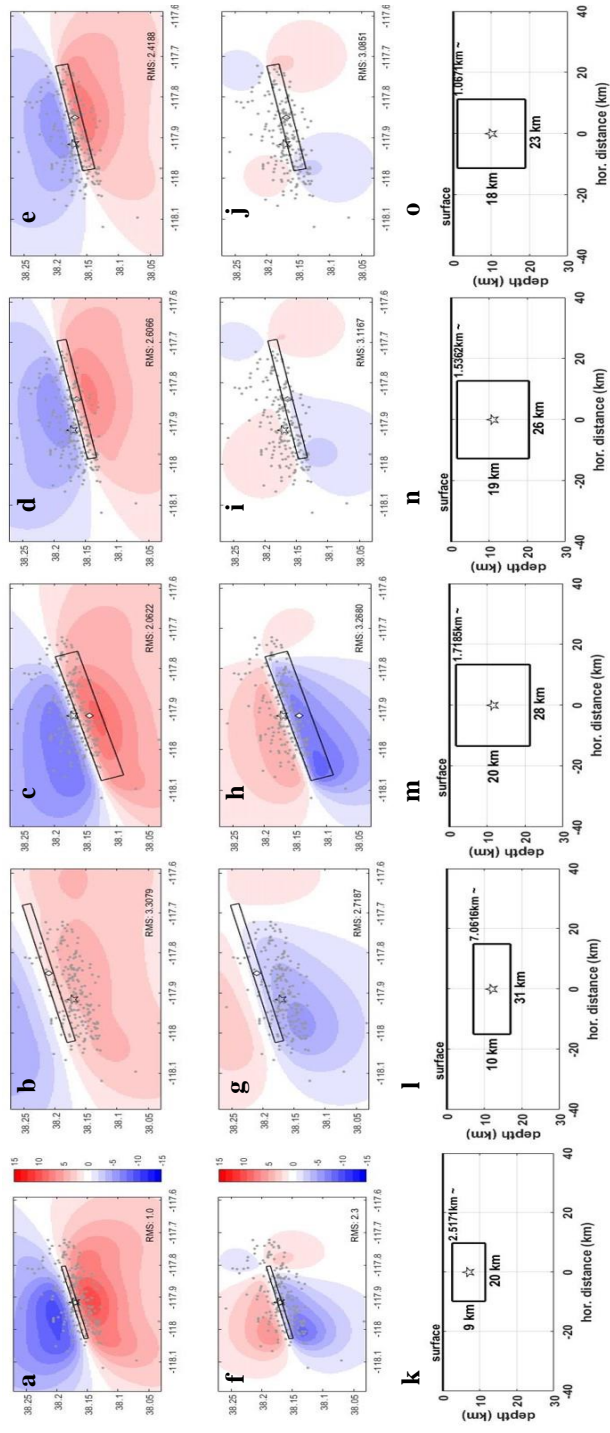


Figure 11. The horizontal (a–e), vertical (f–j) displacement fields, and fault dimension in cross section (k–o) of inferred from InSAR, GCMT, W-phase, Body-wave, NN moment tensor, respectively. The black star represents the epicenter location, the gray dots are aftershock epicenters, and the black lined rectangle is the surface projection of the estimation.

Chapter 5. Discussion and Conclusions

In this study, 3-D coseismic displacement fields of the 2020 Monte Cristo Range earthquake were derived using InSAR data, and the optimal single-segment fault was estimated. The estimation of this study was compared with four moment tensors.

The 3-D coseismic displacement fields from InSAR observations presented in this study were generally in agreement with the results shown in the previous studies. It indicates that Sentinel-1 data processing applied in this study appropriately addressed the limitations of SAR geometry variety. Further, the estimation was also considerably similar to the InSAR observation, especially in the easting displacement field. However, significant subsidence in the observed vertical displacement field was not explained by the model prediction using a single fault segment. It suggests the necessity of further studies considering multi-segment faults to close this misfit.

The result of this study indicates that the left-lateral strike-slip motion is dominant in the earthquake event, as predicted by other moment tensor solutions. The estimated surface motion also supports that the regional tectonic model of Nagorsen-Rinke et al. (2013) would be reasonable to describe the fault system in Mina deflection.

The estimated epicenter location of this study was significantly different to other previous models. The difference is mainly due to the methods using surface displacement and seismic waves. Further, due to the errors in the seismic property model and the wave speed measurement, the displacement fields based on the seismic models

considerably deviate from the observation. The main cause of the difference is an inaccurate epicenter location. In fact, the surface displacement misfits of the seismic models were significantly improved when using the estimated epicenter location of this study.

The estimated depth, strike, dip, and rake are also in agreement well with the previous estimates, except for the seismic moment. The estimated seismic moment of this study was the second smallest. This is due to the smaller fault dimension and the shallow focal depth of the model examined here. The estimated depth of this study was shallower than any other moment tensors. However, as shown in Figure 9, a similar agreement can be obtained from the deeper focal depths and the longer fault width. This trade-off relation would indicate an insensitivity of the depth-dependent parameters.

In conclusion, source parameters derived from InSAR are generally reliable compared to other seismological references, especially in constraining epicenter locations, strike, dip, and rake. It is expected to obtain more accurate source parameters if source parameter studies consider both InSAR and seismic waveform data for various earthquakes.

References

- Aebischer, H.A., & Waldner, S. (1999). A simple and effective method for filtering speckle-interferometric phase fringe patterns. *Optics Communications*, 162, 205-210
- Bennett, R.A., Wernicke, B.P., Niemi, N.A., Friedrich, A.M., & Davis, J.L. (2003). Contemporary strain rates in the northern Basin and Range province from GPS data. *Tectonics*, 22
- Dawson, J., & Tregoning, P. (2007). Uncertainty analysis of earthquake source parameters determined from InSAR: A simulation study. *Journal of Geophysical Research: Solid Earth*, 112
- DeLano, K., Lee, J., Roper, R., & Calvert, A. (2019). Dextral, normal, and sinistral faulting across the eastern California shear zone—Mina deflection transition, California-Nevada, USA. *Geosphere*, 15, 1206-1239
- Ghiglia, D.C., & Romero, L.A. (1994). Robust two-dimensional weighted and unweighted phase unwrapping that uses fast transforms and iterative methods. *Journal of the Optical Society of America A*, 11, 107-117
- Husen, S. & Hardebeck, J.L. (2010). Earthquake location accuracy, Community Online Resource for Statistical Seismicity Analysis
- Kagan, Y.Y. (2003). Accuracy of modern global earthquake catalogs. *Physics of the Earth and Planetary Interiors*, 135, 173-209
- Massonnet, D., Rossi, M., Carmona, C., Adragna, F., Peltzer, G., Feigl, K., & Rabaute, T. (1993). The displacement field of the Landers earthquake mapped by radar interferometry. *Nature*, 364, 138-142

- Nagorsen-Rinke, S., Lee, J., & Calvert, A. (2013). Pliocene sinistral slip across the Adobe Hills, eastern California–western Nevada: Kinematics of fault slip transfer across the Mina deflection. *Geosphere*, 9, 37-53
- Okada, Y. (1985). Surface deformation due to shear and tensile faults in a half-space. *Bulletin of the Seismological Society of America*, 75, 1135-1154
- Oldow, J.S. (2003). Active transtensional boundary zone between the western Great Basin and Sierra Nevada block, western US Cordillera. *Geology*, 31, 1033-1036
- Oldow, J.S., & Craig, S. (1992). Late Cenozoic displacement partitioning in the northwestern Great Basin. In, *Geological Society of Nevada Walker Lane symposium: Structure, tectonics and mineralization of the Walker Lane: Reno, Geological Society of Nevada* (pp. 17-52)
- Oldow, J.S., Kohler, G., & Donelick, R.A. (1994). Late Cenozoic extensional transfer in the Walker Lane strike-slip belt, Nevada. *Geology*, 22, 637-640
- Reid, H.F. (1910). Mechanics of the earthquake, the California Earthquake of April 18, 1906. *Report of the State Investigation Commission*
- Sadeghi Chorsi, T., Braunmiller, J., Deng, F., Mueller, N., Kerstetter, S., Stern, R.J., & Dixon, T.H. (2022). The May 15, 2020 M 6.5 Monte Cristo Range, Nevada, earthquake: eyes in the sky, boots on the ground, and a chance for students to learn. *International Geology Review*, 64, 2683-2702
- Simons, M., Fialko, Y., & Rivera, L. (2002). Coseismic Deformation from the 1999 Mw 7.1 Hector Mine, California, Earthquake as Inferred from InSAR and GPS Observations. *Bulletin of the Seismological Society of America*, 92, 1390-1402

- Stein, S., & Wysession, M. (2003). *Introduction to Seismology, Earthquakes, and Earth Structure*. Blackwell Publishing
- Statista Search Department (2022, July) The 10 most significant natural disasters worldwide by death toll from 1980 to July 2022 [Infographic]. Statista.
<https://www.statista.com/statistics/268029/natural-disasters-by-death-toll-since-1980/>
- Tang, H., & Sun, W. (2018). Closed-Form Expressions of Seismic Deformation in a Homogeneous Maxwell Earth Model. *Journal of Geophysical Research: Solid Earth*, 123, 6033-6051
- Magnitude Types by Earthquake Hazards Program. U.S. Geological Survey.
<https://www.usgs.gov/programs/earthquake-hazards/magnitude-types>
- Wright, T.J., Lu, Z., & Wicks, C. (2003). Source model for the Mw 6.7, 23 October 2002, Nenana Mountain Earthquake (Alaska) from InSAR. *Geophysical Research Letters*, 30
- Zheng, A., Chen, X., & Xu, W. (2020). Present-Day Deformation Mechanism of the Northeastern Mina Deflection Revealed by the 2020 Mw 6.5 Monte Cristo Range Earthquake. *Geophysical Research Letters*, 47, e2020GL090142

국문요약

InSAR 를 이용한 2020 Monte Cristo Range 지진의 진원 파라미터 추정

서울대학교 대학원

과학교육과 지구과학 전공

김 신 애

지진으로 인한 피해를 최소화 하기 위해서는 진원 파라미터를 파악하고 지진의 메커니즘을 이해할 필요가 있다. 여러 진원 파라미터를 추정하는 방법 중 InSAR 는 단층으로 인한 지표의 변위를 측정하여 진원 파라미터를 알아내는 데 활용된다. 본 연구에서는 2020 년 미국 네바다주에서 일어난 Monte Cristo Range 지진의 InSAR 데이터를 통해 지표의 3 차원 변위장을 계산하고, 이러한 변위장을 만들어낸 단층의 진앙, 주향, 경사, 길이, 너비, 진원의 깊이를 몬테카를로 방법을 이용하여 추정하였고, 슬립 벡터는 단층 모델을 이용한 역산을 이용하여 추정하였다. InSAR 로 추론한 본 지진을 일으킨 단층의 종류는 좌수향 주향 이동 성분이 우세한 사교 이동 단층으로 지진파를 이용하여 얻은 진원 파라미터와 비교했을 때 주향, 경사, 면선각이 상당히 일치했고, 진앙은 지진파를 이용하여 얻은 진앙에 비해 관측된 지표 변위장과의 오차가 적은 것을 확인하였다. 최적의 진원 깊이나 모멘트는 지진파를 이용하여 얻은 진원 파라미터와 비교했을 때 작게 나왔지만 진원의 깊이를 증가시키는 경우, 단층의 너비가 함께 증가하면서 최적의 추정치와 비슷한 오차를 보이는 것을 확인하였다. 이번 연구로 지진 파라미터 추정에 InSAR 가 유용하게

활용될 수 있음을 확인하였고, 앞으로 다양한 지진에 대해서 InSAR 와 지진파를 통하여 추론한 진원 파라미터를 함께 비교 연구한다면 더욱 정확한 진원 파라미터를 얻을 수 있을 것이라 기대된다.

주요어: 지진, InSAR, 진원 파라미터, 역산

학 번: 2019-22192